Investigating nano-precipitation in a V-containing HSLA steel using small angle neutron scattering

Wang, YQ, Clark, SJ, Janik, V, Heenan, RK, Venero, DA, Yan, K, McCartney, DG, Sridhar, S & Lee, PD

Original citation & hyperlink:
Wang, YQ, Clark, SJ, Janik, V, Heenan, RK, Venero, DA, Yan, K, McCartney, DG, Sridhar, S & Lee, PD 2018, 'Investigating nano-precipitation in a V-containing HSLA steel using small angle neutron scattering' *Acta Materialia*, vol 145, pp. 84-96
https://dx.doi.org/10.1016/j.actamat.2017.11.032

DOI 10.1016/j.actamat.2017.11.032
ISSN 1359-6454

Publisher: Elsevier

Investigating nano-precipitation in a V-containing HSLA steel using small angle neutron scattering

Y. Q. Wang[a, b], S. J. Clark[c], V. Janik[c, d], R. K. Heenan[e], D. Alba Venero[e], K. Yan[a, b], D. G. McCartney[b, f], S. Sridhar[c, g], P. D. Lee[a, b]

[a] *School of Materials, University of Manchester, Manchester, M13 9PL, UK*

[b] *Research Complex at Harwell, Rutherford Appleton Laboratory, Harwell, OX11 0FA, Oxfordshire, UK*

[c] *WMG, University of Warwick, Coventry, CV4 7AL, UK*

[d] *Faculty Research Centre for Manufacturing and Materials Engineering, Coventry University, Coventry, CV1 5FB, UK,*

[e] *Rutherford Appleton Laboratory, Didcot, Oxfordshire, OX11 0QX, UK*

[f], *Advanced Materials Group, University of Nottingham, Nottingham, NG7 2RD, UK*

[g], *George S. Ansell Department of Metallurgical and Materials Engineering, Colorado School of Mines, Golden, CO 80401, USA*

Abstract

Interphase precipitation (IPP) of nanoscale carbides in a vanadium-containing high-strength low-alloy steel has been investigated. Small angle neutron scattering (SANS) and transmission electron microscopy (TEM) were employed to characterize the precipitates and their size distributions in Fe-0.047C-0.2V-1.6Mn (in wt.%) alloy samples which had been austenitized, isothermally transformed at 700 °C for between 3 and 600 min and water quenched. TEM confirms that, following heat treatment, rows of vanadium-containing nanoscale interphase precipitates were present. Model-independent analysis of the nuclear SANS signal and model fitting calculations, using oblate spheroid and disc-shapes, were performed. The major axis diameter increased from 18 nm after 3 min to 35 nm after 600 min. Precipitate volume percent increased from 0.09 to 0.22 vol% over the same period and number density fell from 2×10^{21} to 5×10^{20} m^{-3}. A limited number of measurements of precipitate maximum diameters from TEM images showed the mean value increased from

8 nm after 5 min to 28 nm after 600 min which is in reasonable agreement with the SANS data.

Key Words: Microalloyed steel, Precipitation, Small angle scattering, Transmission electron microscopy

1. Introduction

High-strength, low-alloy (HSLA) steels which contain typically 0.05 to 0.15 wt%C, up to 2 wt%Mn and small (microalloy) additions of elements Mo, Nb, Ti and V (all usually <0.2wt%) have been in use as rolled sheet for automotive products for a number of years [1-6]. These small additions can form carbo-nitride (MX) (M =Mo,Nb,V,Ti and X = C,N) precipitates having the B1 (Fm3m) NaCl-type, FCC structure within the BCC ferrite (α-Fe) matrix [3].

However, there is a significant need to reduce the weight of automobiles in order to improve vehicle efficiency and achieve reduced fuel consumption and emissions. At the same time, passenger safety must not be compromised and so there is a growing demand from the automotive industry for highly formable steels with increased strength [7, 8]. This demand has led to intensive research and a growth in the production of steels that offer improved property combinations. These are termed advanced high strength steels (AHSS). The major difference between HSLA steels and AHSS is that the former have predominantly ferritic microstructures with a small volume fraction of microalloy carbonitride precipitates whereas the latter comprise dual phase (DP) steels (e.g. ferrite plus martensite) and steels that exhibit phenomena such as transformation induced and twinning induced plasticity. Nonetheless, there are some important differences between the mechanical behaviours of DP steels and predominantly single phase steels which are precipitation strengthened [9].

For example, it has been reported that the local elongation of DP steels, such as is required for hole expansion operations in manufacturing, is lacking in DP alloys. In response to this need, Funakawa et al.[10] reported the development of a new type of hot rolled steel that is based on a composition which gives rise to a ferrite matrix with nanometre-sized microalloy

carbides. The latter are formed via the well-known interphase precipitation mechanism in which rows and sheets of nanometre scale MX precipitates form at a moving α/γ interface during either isothermal transformation or continuous cooling and their very fine scale leads to a large precipitation hardening effect [2, 10-19]. The steel composition and processing conditions need to be carefully selected to avoid the formation of pearlite or cementite which would degrade formability [10].

In this context, there has been renewed interest in the topic of interphase precipitation (IPP), first investigated more than 40 years ago, as a means of introducing precipitates that are typically 5-15 nm in diameter, with rows that are ~ 30 to 50 nm apart. Vanadium carbide is often selected as an interphase precipitate because the solubility product of VC in austenite is much larger than that of TiC or NbC [20]. Therefore, it has little tendency to precipitate in the γ phase but instead precipitates during cooling so that a relatively large amount of precipitation occurs in the α-ferrite. However, maintaining a fine precipitate size during steel processing (i.e. prevention of precipitate coarsening by Ostwald ripening) is crucial to achieving a sufficiently large precipitation hardening effect in the final product. Vanadium carbide has a relatively high coarsening rate and consequently, significant attention has also been given to the investigation of Ti and Ti-Mo-containing steels. Both systems exhibit IPP but it has been found that the coarsening of carbide precipitates is significantly retarded in Ti-Mo alloys [14, 21-25].

Previous studies of IPP have included topics such as the effect of transformation temperature [11, 15, 26], time [27], cooling rate [16, 28-30], orientation relationship [15, 31-35], hot deformation [17, 36] as well as the addition of Mo [10, 14, 21-25] on precipitate composition, size, morphology and number density. The majority of these prior studies have used transmission electron microscopy (TEM) to characterise the precipitates [14, 18, 19, 22, 37, 38]. More recently atom probe tomography (APT) [15, 35, 39, 40] has been employed to

directly measure the composition, morphology, and size of individual precipitates. However, obtaining reliable statistical data on particle size distributions, chemical composition, morphology and volume fractions following IPP is a particular challenge as IPP typically occurs inhomogeneously [15, 35, 41]. TEM and APT both have a limited capability to analyse statistically significant numbers of precipitates efficiently which limits our ability to predict mechanical properties via models of precipitate - dislocation interactions. The lack of representative data on precipitates from significant volumes of bulk material, including factors such as size and spacing, also restricts the development of new and improved models of interphase precipitation [18, 42-49]. Improved, statistically significant, data on the size and distribution of interphase precipitates from bulk samples are thus needed.

Small angle scattering techniques based on neutrons or X-rays are potentially suitable for acquiring bulk-scale, statistically sound data on fine scale IP precipitates of the MX type in HSLA steels. Small angle neutron scattering (SANS) is generally preferred and over the past twenty years, there has been a growing interest in its use to measure the size, size distribution and volume fraction of nanoscale precipitates in various types of steel. This has included studies at room temperature on strip cast low carbon steels [37, 50, 51], maraging and martensitic steels [52, 53], Ti and Nb-containing microalloyed steels [54-57], Nb-containing pipeline steels [58] and NbC precipitation in the austenite phase [59]. Although Oba et al. [60] investigated IPP in a vanadium microalloyed steel, this was a medium-carbon grade and quantitative data on IPP in low-carbon, V- microalloyed steels have not apparently been reported.

The overall purpose of the present work was to use SANS to quantitatively analyze the size and volume fraction of IP precipitates and to investigate the changes occurring during isothermal transformation. A steel of composition Fe-0.047C-0.2V-1.6Mn (in wt.%) was selected for the present investigation because V is the most soluble of the microalloying elements in austenite (γ) at high temperature and it does not readily precipitate in the γ-phase

during cooling making it a very suitable addition for the formation of IP precipitates. In the present study, we measured precipitate characteristics from both the magnetic and the nuclear scattering signals and correlated the measurements with electron microscope observations and microhardness data. The results will aid modelling of precipitation strengthening and in the selection of suitable thermomechanical processing schedules for controlled IPP, with a SANS methodology extendable to a wider range of ferromagnetic alloys.

2. Materials and methods

2.1 Materials

A V-containing, microalloyed low-carbon steel provided by Tata Steel Europe was employed. The composition of the alloy, as determined by chemical analysis, is given in Table 1. The alloy was prepared by vacuum induction melting and cast into ingots with dimensions of 350 x 105 x 100 mm. These ingots were forged at approximately 1250 °C to a final thickness of 35 mm (i.e. a reduction of 65 %) and air cooled. To ensure that the thermomechanical processing was relevant to that employed in industrial operations, the additional 2-3 day homogenization stage at high temperature used in some prior studies on other alloys, was not applied. Six samples (with dimensions of 30 × 10 × 6 mm) were machined from the forgings and austenitized in a salt bath at 1150 °C for 5 min. One of the samples was water quenched directly from 1150 °C. The remaining samples were transferred directly to another salt bath and held at 700 °C for periods in the range 3 min to 600 min and water quenched (see Supplementary Data). Approximately 0.5 mm was removed from the surfaces prior to SANS analysis or further sample preparation for microscopy.

2.2 Materials characterization

Samples were sectioned and metallographically prepared by the normal methods. Scanning electron microscopy (SEM) was conducted using an FEI Quanta 650 FEG-SEM operated at a

voltage of 20 kV. Specimens were given a final polish with a colloidal silica suspension (OPS) and etched with 2% Nital.

For examination in the transmission electron microscope (TEM), samples were prepared by mechanical grinding/polishing to 50 µm thickness and then twin-jet electro-polished in a solution of 10 vol.% $HClO_4$ mixed with 90 vol.% CH_3COOH at approximately -15°C. TEM observations were performed using a JEOL 2100 scanning TEM operating at 200 kV equipped with 80 mm^2 silicon drift EDS detector (SDD) Oxford Instruments X-Max; aperture size 5 nm was used for STEM-EDS acquisition. Additionally, to examine in more detail the sample heat-treated for 600 min, an FEG-TEM FEI Talos F200X operating at 200 kV with four integrated Super-X SDD EDS detectors at a detection angle of 0.9 srad was used for high resolution imaging and elemental mapping of vanadium. In this case, a modified focused ion beam (FIB) lift-out method was used to prepare foils ~120 nm in thickness. The modified FIB preparation procedure involved an initial standard sample lift out preparation with 25 kV Ga-ions followed by a final low energy Ga-ion milling at 500 V and at an angle of 12° on both sides of the TEM foil sample [61]. This was designed to minimise the level of ion-induced damage due to surface re-deposition, amorphisation and implantation and to allow accurate observation of nano-scale features.

The average precipitate diameters in the samples aged for 5 min and for 600 min were measured from bright field TEM images and STEM-EDS maps by exporting them to ImageJ software [62]. Assuming that all precipitates have either oblate spheroid or disc-shaped morphologies an individual particle diameter was calculated as being equal to the calibrated diameter of the major axis (long axis) on the image plane. For each ageing condition, a minimum of 300 precipitates, both random and interphase, were analysed from a total of 20 TEM images.

153 The microhardness (Hv) of isothermally transformed samples was measured using a Wilson
154 VH3100 microhardness tester with a load of 0.1 kgf. In partially transformed samples,
155 indents were placed only within the ferrite grains. The mean value of 25 measurements is
156 reported and the error is given as one standard deviation.

157 **2.3 SANS experiment method**

158 Small angle neutron scattering (SANS) experiments were performed on the SANS2d
159 beamline at the ISIS Pulsed Neutron Source, UK [63]. A schematic of the experimental setup
160 is shown in Fig. 1. Small angle scattering arises from nanoscale precipitates embedded in the
161 ferritic matrix (as shown in Fig. 1a and 1b) as well as larger scale structural features. A
162 magnetic field of 1.5 T was applied in a horizontal direction parallel to the sample surface (i.e.
163 perpendicular to the neutron beam) sufficient to saturate the α-Fe matrix and suppress
164 multiple scattering. Polychromatic neutrons (λ=1.7 to 16.5 Å) were used but only
165 wavelengths in the range of 4.7 to 16.5 Å were selected for data analysis in order to avoid
166 multi-Bragg diffraction [64-66]. Samples of approximately 10 mm × 10 mm × ~1 mm
167 (thickness) were polished to 1 µm diamond surface finish and exposed for 60 min to a
168 neutron beam of 8 mm diameter. The detector configuration gave a small angle scattering
169 vector (q) range of 0.004 to 0.3 $Å^{-1}$, where $q = 4\pi sin\theta/\lambda$ and the scattering angle is 2θ.
170 Absolute SANS intensities were obtained using standard procedures [5, 67]. Nuclear and
171 "nuclear plus magnetic" scattering cross-sections were obtained by partial azimuthal
172 averaging in 30° sectors around the transmitted beam as shown in Figure 1(c) leading to one-
173 dimensional plots of scattering intensity, I, versus q (Figure 1(d)). (Further details in
174 Supplementary Data).

175 **3. SANS data reduction and analysis method**

176 If the precipitates are assumed to be non-interacting particles then the SANS scattering
177 intensity, I, of the particle dispersion is given by

$$I(q) = (\Delta\rho)^2 \int_0^\infty N(r)V(r)^2F(q,r)^2\,dr \qquad (1)$$

where Δρ is the difference in the scattering length densities of the particle and the matrix, *N(r)dr* is the number density of particles with size between *r* and *r+dr, V(r)* is the volume of a particle of size *r* and *F(q,r)* is the form factor for the particles and *q* is the scattering vector [66, 68, 69].

Neutron scattering contrast has both a magnetic, $\Delta\rho_{mag}$, and a nuclear, $\Delta\rho_{nuc}$, contributions. In a field that magnetizes the matrix to saturation, *I(q)* depends on the angle ϕ between the scattering vector and the magnetic field. Thus $\Delta\rho$ in eqn. 1 can be written as

$$(\Delta\rho)^2 = (\Delta\rho_{nuc})^2 + \left(\Delta\rho_{mag}\right)^2 sin^2\phi \qquad (2)$$

Fig. 1c shows an example of a two dimensional detector image arising from this effect. The nuclear scattering intensity is measured along $\phi = 0^\circ$ and the sum of nuclear and magnetic scattering along ϕ = 90°. To produce one-dimensional scattering profiles (Fig. 1(d)) we employed azimuthal data integration from -15<ϕ<+15° to determine nuclear scattering and between 75<ϕ<+105° to find nuclear plus magnetic scattering.

When the matrix is magnetized to saturation, and the chemical size of the precipitates is the same as their magnetic size, the ratio *R*(*q*) depends on their chemical composition through the dependence of $\Delta\rho_{nuc}$ on precipitate chemistry.

$$R(q) = \frac{I_{mag}(q)}{I_{nuc}(q)} = \left(\frac{\Delta\rho_{mag}}{\Delta\rho_{nuc}}\right)^2 \qquad (3)$$

If all precipitates have the same composition then *R*(*q*) is constant. However, *R*(*q*) will vary if either there is more than one type of precipitate present of differing size or the precipitate composition is size dependent [54].

Our model independent analysis (assuming disc-shaped IP precipitates) of particles is based on the Guinier, Kratky and Porod representations of the absolute scattering intensity data and follows standard methods [68-70].

A radius of gyration, R_{g1}, is calculated from the Guinier plot (which takes the form of ln(*I) vs* q^2) using a self-consistent method with $1<qR_{g1}<2$.

For a distribution of monodisperse thin discs of thickness, *T*, and radius, *R*, the relationship between *T*, *R* and R_{g1} is given by [70]

$$R_{g1}^2 = \frac{T^2}{12} + \frac{R^2}{2} \quad (4)$$

A second Guinier plot of $\ln[q^2(I)]$ vs q^2 is known to give a radius of gyration, R_{g2}, that is related to the thickness, *T*, of a disc.

$$R_{g2} = \left(\frac{T^2}{12}\right)^{1/2} \quad (5)$$

However, for polydisperse distributions there is not a simple relationship between R_{g1}, R_{g2} and mean particle dimensions as discussed in detail by Deschamps and De Geuser [69].

In the Kratky plot, Iq^2 is plotted versus q and a characteristic particle size, R_{max},(the "pseudo Guinier radius",) can be determined from the maximum, q_{max}, in the plot [69].

$$R_{max} = \frac{\sqrt{3}}{q_{max}} \quad (6)$$

The volume fraction of precipitate, f_v, in a dilute incompressible two-phase system is also obtained from the Kratky plot. The integrated small angle scattering, Q, (i.e. the Porod invariant) is given by

$$Q = \int_0^\infty I(q) q^2 \, dq = 2\pi^2 (\rho_p - \rho_m)^2 f_v (1 - f_v) \quad (7)$$

where ρ_p and ρ_m are the scattering length densities (either nuclear or magnetic) of precipitate and matrix respectively. The q-range for integration was extrapolated to 10^{-5} Å^{-1} for low q and 10 Å^{-1} for high q with the Guinier equation and the Porod law respectively as recommended in reference [66]. Thus f_v can be found using the data in Supplementary Note 3.

A model fitting analysis was also carried out based on physical understanding from the model-independent analysis and using the SasView software program [71]. Two kinds of form factor fitting functions were investigated based on precipitates being assumed to be either disc or an oblate ellipsoid of revolution shape (i.e. an oblate spheroid).

In the case of a disc, the form factor is given by

$$F_{disc}(q,R,T) = \frac{2J_1(qRsin\alpha)}{qRsin\alpha}\frac{sin(qTcos\alpha)}{qTcos\alpha} \quad (8)$$

where α is the angle between the axis of the thin disc, q the scattering vector, T the thickness of the disc and R is the radius. J_1 is a first order Bessel function.

For the ellipsoidal shape, the form factor becomes

$$F_{ellipsoid}(q,a,b) = 3\frac{sin[qr(a,b,\alpha)]-cos[qr(a,b,\alpha)]}{(qR)^3} \quad (9)$$

$$\text{where } r(a,b,\alpha) = (asin^2\alpha + bcos^2\alpha)^{0.5} \quad (10)$$

α is the angle between the axis of the ellipsoid and q, where b and a are the radii along and perpendicular to the rotation axis of the ellipsoid respectively; b is referred to as the polar axis and a is the equatorial axis.

4. Results and Discussion

4.1. Microstructural characterization

The SEM image of Fig. 2a shows the microstructure of the water quenched alloy which is seen to consist of acicular units, irregularly shaped laths and fine scale precipitates. These features indicate the formation of an auto-tempered martensite and lower bainite. Figs. 2(b)-(f) show the microstructure of samples transformed at 700 °C followed by water quenching. Regions of bainite, which formed from untransformed austenite that was present at the time

of quenching, are evident in Figs. 2(b)-(d). However, bainite is not visible in the samples transformed for 300 min and 600 min (Figs. 2(e) and (f)), indicating that transformation from austenite was complete prior to 300 min of isothermal holding. In the SEM image of Fig. 2(f), IP precipitates are visible within the ferrite grains. These precipitates can be resolved in the SEM because they have coarsened as a result of the long holding time at 700 °C.

Bright field TEM images of the samples transformed at 700°C for 5 min and 600 min respectively are shown in Figs. 3(a) and 3(b). For both transformation times, planar rows of carbide precipitates are observed which indicate that they have most probably been formed by interphase precipitation.

The morphology of the precipitates cannot be fully determined from these two images but is consistent with either a rod or disc-shape. Previous work has reported that IP precipitated vanadium carbides are not spherical but mostly elongated along the $(001)_{VC}$ plane to give an oblate spheroid (i.e. disc-shaped) morphology. This occurs because the $(001)_{VC}$ plane is a habit plane of VC and parallel to (001) plane in the ferrite [19, 72]. Therefore, in this study we assume that the vanadium carbides also exhibit such a morphology. Figs. 3(c) and 3(d) show representative high resolution TEM lattice images of the carbide precipitates in the sample held for 600 min. The long axis diameter of the precipitates are around 21 nm to 28 nm. The EDX map (Fig. 3(e)) confirms the precipitates are V-rich.

Precipitate size measurements, performed as described in section 2.2 on TEM images and EDX maps, give a mean value for the long axis carbide diameter. After 5 min ageing, this was found to be 7.8±3.6 nm and after 600 min ageing it was 27.8±8.0 nm (where the errors correspond to the standard deviation in the data). The long axis measurement is consistent with the HR-TEM lattice image and the change in long axis diameter with ageing time indicates a significant coarsening effect.

4.2 Interpretation of small angle neutron scattering measurements

One-dimensional plots of intensity versus scattering vector extracted from the SANS data for the water quenched and isothermally transformed (3, 60 and 300 min) alloys are shown in Figs. 4(a)-(d) respectively. In the water quenched sample, only the nuclear signal closely follows a q^{-4} variation (i.e. the Porod Law) over the entire q-range until the background level is reached at q>0.1 Å^{-1}. This shows that the principal contribution to nuclear scattering is from the interface between scattering particles and the matrix where the particles are large scale features typically > $2\pi/q_{min}$ (approx. 150 nm). These will typically be alloy carbides, nitrides or sulphides formed during steel manufacture. The iron carbides present in the bainitic regions of the quenched alloy (Fig. 2(a)) make negligible contribution to the nuclear scattering pattern because of their small contrast factor (See Supplementary Data). If nanoscale VC precipitates had formed they would contribute strongly to the nuclear signal due to their large contrast factor and so the q^{-4} behaviour of the nuclear signal indicates that there is no detectable nanoscale VC present following austenitization and quenching. However, the magnetic scattering signal deviates significantly from a q^{-4} behaviour over the range 0.004<q<0.05 Å^{-1} because magnetic scattering is significant from iron carbide precipitates (they are not ferromagnetic and behave as magnetic "holes" in the matrix).

The SANS results obtained from the isothermally transformed samples which were water quenched following transformation times of 3, 60, and 300 min are also shown in Fig. 4. In Fig. 4(b) both magnetic and nuclear scattering intensities deviate from a q^{-4} Porod-type behaviour. In the case of the nuclear signal, the deviation at q ~ 0.01 Å^{-1}arises from the formation of nanoscale ($d \leq 50$ nm) VC precipitates, formed during the isothermal hold as seen in the TEM images of Figs. 3. The magnetic signal shows a different behaviour to the nuclear one due to the presence of residual islands of transformed austenite (i.e. bainite) (Figs. 2(b)-2(d)) which contain iron carbides. The magnetic signal thus has contributions from both the nanoscale VC and the somewhat larger iron carbide phases giving rise to a deviation from q^{-4} behaviour at lower values of the scattering vector q (larger values of particle size). Fig. 4(c)

297 shows similar features to Fig. 4(b) but the difference between nuclear and magnetic signals is
298 diminished due to the reduced fraction of bainite in the microstructure following 60 min
299 transformation followed by quenching, giving a reduced quantity of iron carbide compared to
300 the shorter ageing time. The magnitude of the nuclear signal is evidently increased as a result
301 of a greater phase fraction of VC and the signal covers a larger range of scattering vector, q.
302 Following 60 min transformation, the nuclear and magnetic signals are similar, consistent
303 with the very small volume fraction of bainite seen in Fig. 2(d). In Fig. 4(d), the nuclear and
304 magnetic signals have a similar magnitude over the entire q range following 300 min
305 transformation. Two factors contribute to this. First, the nuclear and magnetic contrast factors
306 of VC are similar (Supplementary Data). Secondly, isothermal transformation of austenite to
307 ferrite was complete following a 300 min hold and hence there was no additional scattering
308 contribution from iron carbides. Thus the large overall scattering signal above the Porod
309 background is due to the nanoscale VC precipitates as seen in the TEM images of Fig. 3. The
310 1-D pattern for the sample transformed for 600 min is not shown but it has very similar
311 features to Fig. 4(d) and is given in Supplementary Data.
312 Figure 5 shows the ratio of magnetic to nuclear scattering ($R(q)$ versus q, equation 3) for the
313 water quenched and isothermally transformed samples. For the water quenched sample, the
314 plot has a maximum value of 10.5 at $q \sim 0.04$Å. This implies the magnetic scattering signal
315 was raised by iron carbide particles ranging in size from 15 to 150 nm. The dependence of
316 $R(q)$ on q decreased significantly with increasing transformation time and the maximum
317 value of $R(q)$ shifted to smaller q values indicating an increase in the size of the iron carbides
318 in the bainite formed on quenching as well as the formation of a second type of precipitate
319 with a much lower $R(q)$ value, presumably the vanadium carbide precipitates.
320 The austenite to ferrite transformation was completed in the samples transformed for 300 and
321 600 min and the corresponding values of $R(q)$ are almost independent of q and close to 1.
322 This is consistent with the formation of a single V-containing carbide, the composition of

which is independent of size. However, the mean value decreases slightly with transformation time (Table 2), which could be due to the mean carbide composition changing with time.

4.3 Determination of precipitate characteristics and the effect of transformation time

Further analysis of the changing VC volume fraction, size and size distribution during isothermal transformation is based on the 1-D nuclear data shown in Fig. 4, with the removal of (i) the effect of Porod Law scattering (large particles) and (ii) the incoherent background [66]. Figure 6(a) shows the intensity, I, versus scattering vector, q, the Kratky representation (Iq^2 versus q) is shown in Fig. 6(b), Fig. 6(c) is the first Guinier representation ($ln(I)$ versus q^2) and Fig. 6(d) is the second Guinier representation ($ln(q^2I)$ *vs* q^2).

Principal features of the I(q) versus q plots

It is clear from Fig. 6(a) that the I versus q^n power law exponents depend on the q range. At low q (region I) and high q (region III) ranges, the exponent is found to have values of 0 and -4 respectively. The exponent zero corresponds to the Guinier regime which probes real space regions of size q^{-1}; ie regions >> precipitate sizes [73]. The exponent -4 relates to the Porod regime which probes the interfaces between the precipitate and the matrix. The scattering intensity is related to the precipitate surface area per unit volume. The intermediate q region (II) follows an exponent of approximately -2 as indicated in Fig. 6a. In this regime, the slope is related to the shape of the precipitate and q^{-2} indicates that the precipitates are thin discs or oblate spheroids [74] and so this slope is consistent with the precipitate morphology observed in the TEM images (Fig. 3).

Precipitate size and precipitate volume fraction calculated from Kratky plot

The Kratky plots of Iq^2 versus q (where I is the nuclear intensity) for samples transformed for different times are shown in Fig. 6(b). These plots provide a visual indication of volume fraction and size of the VC precipitates. The precipitate volume fraction is calculated from

the area under the Kratky plot (equation 7) whilst, q_{max} (equation 6) provides an estimate of the particle size which is termed the pseudo-Guinier radius, $R_{max.}$ Numerical curve fitting was used to find q_{max} and R_{max} values. The values obtained for volume fraction, $f_{v,}$ and R_{max} are listed in Table 2 and it is evident that both of these increase with transformation time. The different sets of values for f_v arise from the different assumptions made in applying Eq. (7). In one case, it was assumed that the precipitate had the stoichiometric VC composition giving a constant nuclear contrast factor in the calculation of f_v. In the other case, a mean $R(q)$ value (taken from Fig. 5) was used to calculate the nuclear contrast factor on the assumption of a constant magnetic contrast factor (see Supplementary Data). It was only possible to perform mean $R(q)$ estimates for the fully transformed samples i.e. the 300 and 600 min transformation times. The values obtained from the constant nuclear contrast calculation probably represent an upper-bound value for f_v.

Considering now the interpretation of the pseudo-Guinier radius $R_{max,}$ it is shown in reference [69] that the relationship between R_{max} and the mean particle radius depends on both the value of the dispersion parameter and also on the aspect ratio of the precipitate. Despite this limitation, the increase in R_{max} with transformation time shown in Table 2 suggests a marked coarsening behaviour of the precipitate population with the transformation time when held at 700 °C.

Precipitate size calculated from Guinier plot

Plots of the Guinier equations used to derive R_{g1} ($ln(I)$ *vs* q^2) and R_{g2} ($ln(q^2(I))$ *vs* q^2) from the gradients are displayed in Figs. 6(c) and (d) respectively and values of R_{g1} and R_{g2} are listed in Table 2. In both cases, self-consistent methods were applied for the boundaries of the linear gradient fitting [69]. Clearly, these parameters increase with transformation time, which correlates with the change in R_{max} and indicate a progressive increase in precipitate dimensions.

The limitations of the classical Guinier approach in calculating average particle dimensions for polydisperse systems are well documented [69]. Nonetheless, estimates of disc radius, *R*, and thickness, *T*, of the assumed disc shaped VC precipitates based on the Guinier approach can give valuable size data, recognizing that they represent particle ensemble information, and are given in Table 3 as calculated using equations (4) and (5). These show that both radius and thickness increase significantly and the aspect ratio of the particles is seen to be around 3-4 and changes little with transformation time. The Guinier radii after 5 min and 600 min ageing time of 11.6 nm and 21.7 nm respectively are larger than the mean TEM radius values of 3.9 and 13.9 nm respectively. It is evident that both techniques measure significant coarsening at 700 °C.

Precipitate size calculated from shape dependent model fitting

In order to refine the real-space precipitate size estimates obtained from the SANS data, model fitting was undertaken using the SasView software program [71]. This analysis employed two different precipitate shape models namely a disk shape (radius, R_c, and thickness, T_c, as given in equation 8) and an ellipsoid of revolution (polar axis, *b*, and equatorial axis, *a*, as given in equation 9). An ellipsoid of revolution is also referred to as an oblate spheroid and this term will be used hereafter. The disk model was considered in order to be consistent with the Guinier analysis presented in the previous section whilst the oblate spheroid shape was chosen as this shape has been one that has been assumed in previous work on the IPP of VC studied by TEM e.g. in reference [19]. In both cases, the precipitates were assumed to have a lognormal size dispersion of the major axis (i.e. R_c for the disk and the equatorial axis, *a*, for the oblate spheroid). The magnitude of the dispersion was expressed in terms of the dispersion parameter, σ, which is the standard deviation of the lognormal distribution. The disk thickness and spheroid polar radius were assumed to have a zero dispersion parameter.

The calculated 1-D nuclear scattering profiles were then fitted to the experimental 1-D scattering curves using, as fixed parameters, the precipitate volume fractions, obtained from equation 7, and the contrast between precipitates and ferrite matrix calculated from R(q) (Table 2). The starting estimates in the model for the disk mean radius and half-thickness (major and minor axes respectively in the case of the oblate spheroid) were the *R* and *T* values found from the Guinier analysis. The goodness of fit between experimental and calculated 1-D scattering profiles was determined using the well known chi-squared quantity for all computations. The effect of altering the dispersion parameter in the range 0 to 0.5 was explored and it was found that consistently better fitting was obtained with values of σ in the range 0.1 to 0.3 than for larger values of σ. The Supplementary Data file provides a summary of the calculations for both shapes and for different dispersion values.

As both the disk and oblate spheroid models give acceptable fitting results with very little difference between them for all ageing times, we proceed by reporting the results (mean equatorial radius of particles, *a*, and mean polar radius, *b*) given by the oblate spheroid model for the mid-point polydispersity value, σ=0.2 (there was little difference in goodness of fit for σ in the range 0.1 to 0.3) and refer the reader to the Supplementary Data file for the extended calculations.

Figure 7 shows representative full model fitting plots using the oblate spheroid model with σ=0.2. There is clearly good agreement over the full q-range for all the transformation times. The mean values of particle dimensions obtained from the model calculations are listed in Table 3 (where the dispersion parameter has been taken to be 0.2) along with the values of *R* and *T* determined from the Guinier measurements of Figs. 6(c) and (d). It is evident that there is generally reasonable agreement between *R* and *a* although some larger discrepancies do arise in thickness values at the longest ageing time where the Guinier analysis gives somewhat greater values.

The data listed in Table 3 for the Guinier measurements and the oblate spheroid model fitting are plotted in Fig. 8 and the error bars on the model fitting data points correspond to uncertainties generated from the calculations. Overall, there is seen to be good agreement between particle radius and thickness from the Guinier method calculations and from the model fitting.

Further Discussion

In this section we consider, first, the evidence from the SANS data regarding the composition of the vanadium-containing precipitates and secondly the effect of the particle size and volume fraction on the strengthening contribution of IPP to the ferrite phase.

5.1 Effects of transformation time on composition of MX precipitates

Information on the chemical composition of the precipitates (more generally written as MX where M=V, Fe and X=C,N) can be gained from the ratio $R(q)$ of those samples in which the γ has fully transformed to α and there is no residual martensite or bainite in the microstructure following quenching, i.e. 300 and 600 min transformation times. The mean $R(q)$ decreases from 1.09 to 0.98 (Table 2) suggesting a change in composition of the MX phase. For stoichiometric VC, the value of R(q) from the contrast factors in Supplementary Data is 1.23. The contrast factor for VN is larger than for VC so the substitution of N into the MX phase in place of C cannot provide an explanation for the difference.

Thermodynamically it is feasible for Fe to substitute for V. Using Thermo-Calc and the TCFE 7 database the full equilibrium calculation predicts 0.08 mol%Fe at 700 °C. However, Fe substitution decreases the nuclear contrast factor, increases $R(q)$ and is not a consistent explanation. An alternative to be considered is that the carbide phase is sub-stoichiometric with respect to carbon. This would lead to a higher nuclear contrast factor and hence a reduction in $R(q)$ in line with the experimental measurements.

Assuming a composition $VC_{0.90}$ gives a theoretical $R(q)$ of ~1.1 which is close to the experimental value for the 300 min sample. This value is within the range of possible compositions reported by Baker [2] and several researchers have measured a similar sub-stoichiometry. For example, Oba et al. [60] found that in a medium carbon steel the value of x (x<1) in VC_x is dependent on the transformation temperature whilst Zhang et al. [75] used APT to shows that x is about 0.81 in Fe-0.1C-0.4V alloy isothermally transformed at 690 °C for 48 hours. Furthermore, Ishiguro and Sato [76] used electron energy loss spectroscopy (EELS) to identify non-stoichiometric MC_x in ultra-low carbon microalloy steels with x in the range 0.82 to 0.91. Overall, a sub-stoichiometric vanadium carbide seems a possible explanation for the present $R(q)$ measurements.

5.2 Effect of transformation time on precipitate size and volume fraction

The SANS data clearly demonstrate that changes in size and volume fraction (f_v) of IP precipitates in a low carbon microalloy steel during isothermal ageing at 700°C can be quantified.

There is a steady increase in f_v with transformation time which continues after the γ to α transformation is complete (Table 2 and Fig. 9a) which suggests growth of the carbide from supersaturated ferrite (α). Depending on the assumptions about the scattering length densities, the volume percent after 600 min is in the range 0.22 to 0.28 vol%. This is consistent with the equilibrium volume fraction of 0.30 vol% calculated using Thermo-Calc and the TCFE7 database.

In the present work, it is clear that precipitate dimensions, as represented by Guinier and pseudo-Guinier radii both increase with ageing time at 700 °C. Real space particle dimensions cannot be derived from the above model-independent parameters analytically for polydisperse precipitate distributions [66, 69, 74]. However, from model fitting both an oblate spheroid and disc model are found to give good fits to the data and to be in very

476 reasonable agreement with disc radius and thickness from the Guinier analysis. In Fig. 8,
477 dimensions from Guinier analysis are compared with the oblate spheroid dimensions from
478 model fitting. When the SANS results are compared with the somewhat limited TEM values,
479 the observations of an increase in radius with ageing time agree, as seen in Fig. 8(a) but the
480 TEM values are seen to be consistently smaller than those obtained from SANS. However, it
481 is not surprising that there is a discrepancy since the SANS measurements include orders of
482 magnitude more measurements than the TEM and the SANS measurements will include
483 random and grain boundary precipitates as well as the characteristic aligned rows and sheets
484 of interphase precipitation. Therefore, SANS will tend to measure a larger precipitate size
485 than the TEM method and the latter may well be biased to the IP precipitates with a row and
486 sheet morphology.
487 The measured increase in precipitate radius and thickness with ageing time is consistent with
488 the increasing volume fraction that is measured and is attributed to carbide growth from
489 supersaturated ferrite. To examine whether precipitates also undergo Ostwald ripening
490 (coarsening) the number density, N_v, was calculated based on the mean precipitate volume at
491 each transformation time and the variation of N_v with time is also shown on Fig. 9a.
492 Coarsening (decreasing N_v) is significant when ageing times exceed 60 min (3600 s) which
493 correlates approximately with the completion of the γ to α transformation (i.e. the cessation
494 of nucleation of new carbides by interphase precipitation). N_v is insensitive to whether disc or
495 oblate ellipsoid shapes are considered.
496 Comparison of the present number density data with values reported by Zhang, Kamikawa
497 and co-workers [15, 38, 75] on V-containing microalloy steels is not straightforward due to
498 differences in alloy composition and transformation temperatures and the fact that either
499 TEM or 3DAP were used to arrive at number density values. Zhang et al. [75] used 3DAP
500 and found mean number densities of the order of $5x10^{22}$ m^{-3} for a 0.2wt%V steel transformed
501 for 1 min at 690 °C. Zhang et al. [75] also shows that the number densities of VC increases

approximately 14 times when increase the V content from 0.2 wt% to 0.43 wt%. Kamikawa et al. [38] used TEM and measured interparticle spacing in the range of 44 nm to 78 nm in 0.288 wt%V steels which had been transformed at 690 °C for 5 mins to 300 min at 690 °C. This leads to number densities of 1.2×10^{22} m^{-3} to 2.1×10^{21} m^{-3} which (scaled to the present V content of 0.2wt% according to Zhang et. al.'s study [75]) are from 2.2×10^{21} m^{-3} to 4×10^{20} m^{-3} which agree well with the current SANS studies (Fig. 9a).

5.3 Precipitation strengthening

The strengthening mechanism of IP precipitates and their contribution to the strengthening of ferrite was initially studied by Batte and Honecombe [11]. Subsequent work has shown that the strengthening contribution depends on sheet spacing, particle spacing and particle mean radius [18]. Recently, Kamikawa et al. [14] indicated that the Ashby-Orowan model gave a better fit to IP precipitation strengthening than the Orowan equation [77] and we will apply the former (eqn. 11 below) to the present data

$$\Delta\sigma_{ppt} = \frac{0.538Gbf_v^{0.5}}{2R} ln\left(\frac{R}{b}\right) \qquad (11)$$

$\Delta\sigma_{ppt}$ is the increase in yield strength, G is the shear modulus, b is the Burgers vector, f_v is the carbide volume fraction and R is the mean carbide radius.

The values of $\Delta\sigma_{ppt}$ for the various ageing times are plotted alongside the microhardness data in Fig. 9b and are seen to follow the same trend except at very short times. Microhardness measurements reveal little difference in hardness between the samples aged for 3 and 5 min. The sample aged for 60 min has a hardness which is slightly above those aged for 3 and 5 min but there is a clear and significant decrease in hardness for the longer holding times, suggesting a marked reduction in the resistance to dislocation movement. The decreasing yield strength increment beyond 60 min (3600 s) which is calculated from equation (11) demonstrates that the decrease in ferrite hardness after 60 min is directly influenced by the

increasing particle radius which outweighs the increasing volume fraction of carbide precipitate. In a recent study, Chen et al. [18] measured the IP contribution to ferrite strengthening (in an alloy with 50% more V than in the present material) as 170 to 220 MPa for somewhat lower transformation temperatures. This suggests the values from the simple Ashby-Orowan equation used here are on the low side and that an improved model would require direct microstructural data on sheet spacing and particle spacing that is not available from SANS.

5. Conclusions

Small angle neutron scattering (SANS) was employed to quantify interphase precipitation in samples of a V-containing, low-C microalloy steel which were isothermally transformed at 700 °C for various times followed by water quenching. It is shown to be important to extract both nuclear and magnetic scattering signals so that nanoscale microally carbide precipitates in partially transformed samples can be quantified. Results have been correlated with a microstructural investigation using scanning electron and transmission electron microscopy (TEM).

1. TEM observations confirmed the presence of fine-scale carbide precipitates, rich in V, which exhibited the well-known interphase precipitate morphology of aligned rows and sheets. Precipitates appeared to be either disc or oblate ellipsoid shaped with the mean radius of the major axis increasing from ~4 to ~14 nm as the ageing time increased from 5 to 600 min.
2. Analysis of the nuclear SANS data clearly reveals the presence of the nanoscale precipitates in the isothermally transformed and quenched samples. From Kratky plots, it is clear that the precipitate size and volume percent both increase with transformation time. The latter increased from around 0.09 vol% to a value in the range 0.22 to 0.28 vol% with ageing time.

3. Using simple model-independent Guinier analysis of the 1-D nuclear SANS plots, particle radii (R) and thickness values (T) were calculated. The radii increase with transformation time from ~ 10 to ~ 22 nm. The Guinier analysis was also used to show that the disc shaped precipitates have an aspect ratio of ~3. These values agree well with a model fitting analysis based on an oblate spheroid shape which showed an increased in the radius of the major axis from 9 to 18 nm. The precipitate number density decreases from 2×10^{21} to 5×10^{20} m^{-3} with increasing transformation time when an oblate ellipsoid model is employed for precipitate morphology.
4. The microhardness values of ferrite grains were measured and found to decrease from 215 to 150 Hv as the transformation time increased. They correlate well with the yield strength increments in the range 120 to 90 MPa calculated for different transformation times by using the mean carbide radius in the Ashby-Orowan model.

Acknowledgements

The authors are grateful to Tata steel for providing the experimental materials. This work was made possible via funding from the EPSRC (grants EP/L018705/1, EP/L018632/1, and EP/M009688/1), and the facilities and support provided by the Research Complex at Harwell. The authors gratefully acknowledge the use of the Sans2d beamline, ISIS via RB1520193, RB1620206 and the help provided by colleagues Drs. Chris Simpson and Mark Callaghan. Yiqiang Wang appreciates the useful discussions with Dr Thomas Dorin.

References

[1] F.B. Pickering, Physical Metallurgy and the Design of Steels, Applied Science Publishers, London, 1978.

[2] T.N. Baker, Processes, microstructure and properties of vanadium microalloyed steels, Materials Science and Technology 25(9) (2009) 1083-1107.

[3] T.N. Baker, Microalloyed steels, Ironmaking & Steelmaking 43(4) (2016) 264-307.

[4] J.R. Paules, Developments in HSLA steel products, JOM Journal of the Minerals, Metals and Materials Society 43(1) (1991) 41-44.

[5] G. Platts, A. Vassiliou, F. Pickering, Developments in microalloyed high-strength low-alloy steels: an overview, Metallurgist and materials technologist 16(9) (1984) 447-454.

[6] H. Stuart, The properties and processing of microalloyed HSLA steels, JOM Journal of the Minerals, Metals and Materials Society 43(1) (1991) 35-40.

[7] C.M. Sonsino, Light-weight design chances using high-strength steels, Materialwissenschaft und Werkstofftechnik 38(1) (2007) 9-22.

[8] D. Bhattacharya, Microalloyed steels for the automotive industry, Tecnologia em Metalurgia, Materiais e Mineraçao 11(4) (2014) 371.

[9] A. Kumar, S. Singh, K. Ray, Influence of bainite/martensite-content on the tensile properties of low carbon dual-phase steels, Materials Science and Engineering: A 474(1) (2008) 270-282.

[10] Y. Funakawa, T. Shiozaki, K. Tomita, T. Yamamoto, E. Maeda, Development of high strength hot-rolled sheet steel consisting of ferrite and nanometer-sized carbides, ISIJ international 44(11) (2004) 1945-1951.

[11] A. Batte, R. Honeycombe, Strengthening of ferrite by vanadium carbide precipitation, Metal Science 7(1) (1973) 160-168.

[12] A. Davenport, F. Berry, R. Honeycombe, Interphase precipitation in iron alloys, Metal Science 2(1) (1968) 104-106.

[13] D.P. Dunne, Review: Interaction of precipitation with recrystallisation and phase transformation in low alloy steels, Materials Science and Technology 26(4) (2010) 410-420.

[14] N. Kamikawa, Y. Abe, G. Miyamoto, Y. Funakawa, T. Furuhara, Tensile Behavior of Ti, Mo-added Low Carbon Steels with Interphase Precipitation, ISIJ international 54(1) (2014) 212-221.

[15] Y.-J. Zhang, G. Miyamoto, K. Shinbo, T. Furuhara, T. Ohmura, T. Suzuki, K. Tsuzaki, Effects of transformation temperature on VC interphase precipitation and resultant hardness in low-carbon steels, Acta Materialia 84 (2015) 375-384.

[16] C. Chen, H. Yen, F. Kao, W. Li, C. Huang, J. Yang, S. Wang, Precipitation hardening of high-strength low-alloy steels by nanometer-sized carbides, Materials Science and Engineering: A 499(1) (2009) 162-166.

[17] C.-Y. Chen, J.-R. Yang, C.-C. Chen, S.-F. Chen, Microstructural characterization and strengthening behavior of nanometer sized carbides in Ti–Mo microalloyed steels during continuous cooling process, Materials Characterization 114 (2016) 18-29.

[18] M.-Y. Chen, M. Gouné, M. Verdier, Y. Bréchet, J.-R. Yang, Interphase precipitation in vanadium-alloyed steels: Strengthening contribution and morphological variability with austenite to ferrite transformation, Acta Materialia 64 (2014) 78-92.

[19] G. Miyamoto, R. Hori, B. Poorganji, T. Furuhara, Interphase precipitation of VC and resultant hardening in V-added medium carbon steels, ISIJ international 51(10) (2011) 1733-1739.

[20] R. Lagneborg, T. Siwecki, S. Zajac, B. Hutchinson, The role of vanadium in microalloyed steels, Scand. J. Metall 28(5) (1999) 186-241.

[21] Y. Funakawa, K. Seto, Coarsening behavior of nanometer-sized carbides in hot-rolled high strength sheet steel, Materials science forum, Trans Tech Publ, 2007, pp. 4813-4818.

[22] J. Jang, Y. Heo, C. Lee, H. Bhadeshia, D.-W. Suh, Interphase precipitation in Ti-Nb and Ti-Nb-Mo bearing steel, Materials Science and Technology 29(3) (2013) 309-313.
[23] J.H. Jang, C.-H. Lee, Y.-U. Heo, D.-W. Suh, Stability of (Ti, M) C (M= Nb, V, Mo and W) carbide in steels using first-principles calculations, Acta Materialia 60(1) (2012) 208-217.
[24] W. Lee, S. Hong, C. Park, K. Kim, S. Park, Influence of Mo on precipitation hardening in hot rolled HSLA steels containing Nb, Scripta Materialia 43(4) (2000) 319-324.
[25] W. Zemin, Z. Xiaoyong, L. wenqing, Influence of Mo on tempering precipitation in Nb-Mo-V microalloyed steels, Chinese Journal of Materials research 24(2) (2010) 217-224.
[26] A. Davenport, R. Honeycombe, Precipitation of Carbides at $\ gamma $-$\ alpha $ Boundaries in Alloy Steels, Proceedings of the Royal Society of London A: Mathematical, Physical and Engineering Sciences, The Royal Society, 1971, pp. 191-205.
[27] J. Kim, J.-G. Jung, D.-H. Kim, Y.-K. Lee, The kinetics of Nb (C, N) precipitation during the isothermal austenite to ferrite transformation in a low-carbon Nb-microalloyed steel, Acta Materialia 61(19) (2013) 7437-7443.
[28] F. Bu, X. Wang, L. Chen, S. Yang, C. Shang, R. Misra, Influence of cooling rate on the precipitation behavior in Ti–Nb–Mo microalloyed steels during continuous cooling and relationship to strength, Materials Characterization 102 (2015) 146-155.
[29] H.J. Jun, K. Kang, C. Park, Effects of cooling rate and isothermal holding on the precipitation behavior during continuous casting of Nb–Ti bearing HSLA steels, Scripta Materialia 49(11) (2003) 1081-1086.
[30] S. Clark, V. Janik, A. Rijkenberg, S. Sridhar, Analysis of the extent of interphase precipitation in V-HSLA steels through in-situ characterization of the γ/α transformation, Materials Characterization 115 (2016) 83-89.
[31] N. Law, S. Parsons, P. Howell, D. Edmonds, Crystallography of carbide precipitation at transformation interfaces during austenite decomposition in a low-alloy steel, Materials science and technology 3(8) (1987) 642-648.
[32] R. Okamoto, A. Borgenstam, J. Ågren, Interphase precipitation in niobium-microalloyed steels, Acta Materialia 58(14) (2010) 4783-4790.
[33] H.-W. Yen, P.-Y. Chen, C.-Y. Huang, J.-R. Yang, Interphase precipitation of nanometer-sized carbides in a titanium–molybdenum-bearing low-carbon steel, Acta Materialia 59(16) (2011) 6264-6274.
[34] G. Miyamoto, R. Hori, B. Poorganji, T. Furuhara, Crystallographic analysis of proeutectoid ferrite/austenite interface and interphase precipitation of vanadium carbide in medium-carbon steel, Metallurgical and Materials Transactions A 44(8) (2013) 3436-3443.
[35] Y.-J. Zhang, G. Miyamoto, K. Shinbo, T. Furuhara, Effects of α/γ orientation relationship on VC interphase precipitation in low-carbon steels, Scripta Materialia 69(1) (2013) 17-20.
[36] C. Chih-Yuan, C. Shih-Fan, C. Chien-Chon, Y. Jer-Ren, Control of precipitation morphology in the novel HSLA steel, Materials Science and Engineering: A 634 (2015) 123-133.
[37] T. Dorin, K. Wood, A. Taylor, P. Hodgson, N. Stanford, Effect of coiling treatment on microstructural development and precipitate strengthening of a strip cast steel, Acta Materialia 115 (2016) 167-177.
[38] N. Kamikawa, K. Sato, G. Miyamoto, M. Murayama, N. Sekido, K. Tsuzaki, T. Furuhara, Stress–strain behavior of ferrite and bainite with nano-precipitation in low carbon steels, Acta Materialia 83 (2015) 383-396.
[39] S. Mukherjee, I. Timokhina, C. Zhu, S. Ringer, P. Hodgson, Three-dimensional atom probe microscopy study of interphase precipitation and nanoclusters in thermomechanically treated titanium–molybdenum steels, Acta materialia 61(7) (2013) 2521-2530.

[40] S. Mukherjee, I. Timokhina, C. Zhu, S.P. Ringer, P.D. Hodgson, Clustering and precipitation processes in a ferritic titanium-molybdenum microalloyed steel, Journal of Alloys and Compounds 690 (2017) 621-632.
[41] R. Honeycombe, R. Mehl, Transformation from austenite in alloy steels, Metallurgical Transactions A 7(7) (1976) 915-936.
[42] H. Bhadeshia, Diffusional transformations: A theory for the formation of superledges, physica status solidi (a) 69(2) (1982) 745-750.
[43] P. Rios, Morphology of interphase precipitation in microalloyed steels, Journal of materials science letters 10(16) (1991) 981-983.
[44] W. Liu, Computer simulation of VC, Metallurgical Transactions A 24(10) (1993) 2195-2207.
[45] P. Rios, A model for interphase precipitation in stoichiometrically balanced vanadium steels, Journal of materials science 30(7) (1995) 1872-1878.
[46] R. Lagneborg, S. Zajac, A model for interphase precipitation in V-microalloyed structural steels, Metallurgical and Materials Transactions A 32(1) (2001) 39-50.
[47] M. Ohnuma, J. Suzuki, S. Ohtsuka, S.-W. Kim, T. Kaito, M. Inoue, H. Kitazawa, A new method for the quantitative analysis of the scale and composition of nanosized oxide in 9Cr-ODS steel, Acta materialia 57(18) (2009) 5571-5581.
[48] Toshio Murakami, Hitoshi Hatano, Goro Miyamoto, T. Furuhara, Effects of Ferrite Growth Rate on Interphase Boundary Precipitation in V Microalloyed Steels, ISIJ International 52(4) (2012) 616-625.
[49] M.-Y. Chen, M. Gouné, M. Militzer, Y. Bréchet, J.-R. Yang, Superledge Model for Interphase Precipitation During Austenite-to-Ferrite Transformation, Metallurgical and Materials Transactions A 45(12) (2014) 5351-5361.
[50] T. Dorin, A. Taylor, K. Wood, J. Wang, P. Hodgson, N. Stanford, Complex precipitation phenomena in strip cast steels with high sulfur and copper contents, Journal of Applied Crystallography 49(5) (2016) 1777-1785.
[51] T. Dorin, K. Wood, A. Taylor, P. Hodgson, N. Stanford, Quantitative examination of carbide and sulphide precipitates in chemically complex steels processed by direct strip casting, Materials Characterization 112 (2016) 259-268.
[52] P. Staron, B. Jamnig, H. Leitner, R. Ebner, H. Clemens, Small-angle neutron scattering analysis of the precipitation behaviour in a maraging steel, Journal of applied crystallography 36(3) (2003) 415-419.
[53] G. Albertini, F. Carsughi, R. Coppola, F. Fiori, F. Rustichelli, M. Stefanon, Small-angle neutron scattering microstructural investigation of MANET steel, Journal of nuclear materials 233 (1996) 253-257.
[54] B.S. Seong, E. Shin, S.-H. Choi, Y. Choi, Y.S. Han, K.H. Lee, Y. Tomota, Quantitative analysis of fine nano-sized precipitates in low-carbon steels by small angle neutron scattering, Applied Physics A 99(3) (2010) 613-620.
[55] F. Perrard, A. Deschamps, F. Bley, P. Donnadieu, P. Maugis, A small-angle neutron scattering study of fine-scale NbC precipitation kinetics in the α-Fe–Nb–C system, Journal of applied crystallography 39(4) (2006) 473-482.
[56] H. Yasuhara, K. Sato, Y. Toji, M. Ohnuma, J.-i. Suzuki, Y. Tomota, Size analysis of nanometer titanium carbide in steel by using small-angle neutron scattering, Tetsu To Hagane 96(9) (2010) 545-549.
[57] A. Deschamps, F. Danoix, F. De Geuser, T. Epicier, H. Leitner, M. Perez, Low temperature precipitation kinetics of niobium nitride platelets in Fe, Materials Letters 65(14) (2011) 2265-2268.
[58] J. Wiskel, D. Ivey, H. Henein, The effects of finish rolling temperature and cooling interrupt conditions on precipitation in microalloyed steels using small angle neutron scattering, Metallurgical and Materials Transactions B 39(1) (2008) 116-124.

[59] N. Van Dijk, W. Bouwman, S. Offerman, M.T. Rekveldt, J. Sietsma, S. Van der Zwaag, A. Bodin, R. Heenan, High temperature SANS experiments on Nb (C, N) and MnS precipitates in HSLA steel, Metallurgical and Materials Transactions A 33(7) (2002) 1883-1891.
[60] Y. Oba, S. Koppoju, M. Ohnuma, T. Murakami, H. Hatano, K. Sasakawa, A. Kitahara, J.-i. Suzuki, Quantitative Analysis of Precipitate in Vanadium-microalloyed Medium Carbon Steels Using Small-angle X-ray and Neutron Scattering Methods, ISIJ international 51(11) (2011) 1852-1858.
[61] J. Scott, F.T. Docherty, M. MacKenzie, W. Smith, B. Miller, C.L. Collins, A.J. Craven, Sample preparation for nanoanalytical electron microscopy using the FIB lift-out method and low energy ion milling, Journal of Physics: Conference Series 26(1) (2006) 223.
[62] C.A. Schneider, W.S. Rasband, K.W. Eliceiri, NIH Image to ImageJ: 25 years of image analysis, Nature methods 9(7) (2012) 671-675.
[63] R. Heenan, S. Rogers, D. Turner, A. Terry, J. Treadgold, S. King, Small angle neutron scattering using Sans2d, Neutron News 22(2) (2011) 19-21.
[64] W. Woo, V. Em, E. Shin, P. Mikula, V. Ryukhtin, Influence of multiple small-angle neutron scattering on diffraction peak broadening in ferritic steel, Journal of Applied Crystallography 48(2) (2015) 0-0.
[65] A. Michels, J. Weissmüller, Magnetic-field-dependent small-angle neutron scattering on random anisotropy ferromagnets, Reports on Progress in Physics 71(6) (2008) 066501.
[66] F. De Geuser, A. Deschamps, Precipitate characterisation in metallic systems by small-angle X-ray or neutron scattering, Comptes Rendus Physique 13(3) (2012) 246-256.
[67] G.T. Wignall, F. Bates, Absolute calibration of small-angle neutron scattering data, Journal of applied crystallography 20(1) (1987) 28-40.
[68] O. Glatter, O. Kratky, Small angle scattering, Academic, New York (1982).
[69] A. Deschamps, F. De Geuser, On the validity of simple precipitate size measurements by small-angle scattering in metallic systems, Journal of Applied Crystallography 44(2) (2011) 343-352.
[70] T. Imae, T. Kanaya, M. Furusaka, N. Torikai, Neutrons in soft matter, John Wiley & Sons2011.
[71] SasView, SasView for Small Angle Scattering Analysis. http://www.sasview.org/index.html, 2017 (accessed 4th January 2017.).
[72] N. Kamikawa, M. Hirohashi, Y. Sato, E. Chandiran, G. Miyamoto, T. Furuhara, Tensile Behavior of Ferrite-martensite Dual Phase Steels with Nano-precipitation of Vanadium Carbides, ISIJ International 55(8) (2015) 1781-1790.
[73] F. Cousin, Small angle neutron scattering, EPJ Web of Conferences, EDP Sciences, 2015, p. 01004.
[74] A. Deschamps, F. De Geuser, Quantitative characterization of precipitate microstructures in metallic alloys using small-angle scattering, Metallurgical and Materials Transactions A 44(1) (2013) 77-86.
[75] Y.-J. Zhang, G. Miyamoto, K. Shinbo, T. Furuhara, Quantitative measurements of phase equilibria at migrating α/γ interface and dispersion of VC interphase precipitates: Evaluation of driving force for interphase precipitation, Acta Materialia 128 (2017) 166-175.
[76] Y. Ishiguro, K. Sato, Determination of non-stoichiometric composition of complex carbon-nitrides in steel by measuring plasmon energy, Materials Transactions, JIM 37(4) (1996) 643-649.
[77] T. Gladman, Precipitation hardening in metals, Materials Science and Technology 15(1) (1999) 30-36.

Figure 1. Experimental configuration used in the current SANS measurements. (a) An incident neutron beam transmitted through a specimen containing (b) nano-sized precipitates embedded in a ferritic matrix. (c) The resultant SANS two-dimensional pattern in the presence of a horizontal magnetic field. (d) One-dimensional plot of the 'nuclear+magnetic' and nuclear scattering intensities.

Figure 2. SEM images of the samples isothermally transformed at 700°C for various times and water quenched. (a) directly water quenched; (b) – (d) isothermally transformed for 3, 5 and 60 min respectively showing ferrite grains (F) and regions of bainite (B) (transformed γ). (e) and (f) 300 and 600 min isothermal transformation times respectively. Coarsened interphase precipitates visible in (f).

Figure 3, Bright field TEM images of periodic interphase precipitation taken from the samples isothermally transformed at 700°C for (a) 5 min and (b) 600 min. (c-d) High resolution TEM lattice image from the sample held for 600 min, (d) elucidating the disc nature of the precipitates and (e) EDX map for V.

Figure 4. One-dimensional SANS patterns of intensity versus scattering vector obtained from the following samples: (a) water-quenched and (b) to (d) isothermally transformed. Transformation times of: (b) 3 min, (c) 60 min, (d) 300 min. In (a)-(c) there is a clear difference between nuclear and magnetic signals. In (d) they are virtually identical. Line of slope -4 is shown for reference on the log-log plot.

Figure 5. Plot of $R(q)$ versus scattering vector calculated from the scattering curves in Fig. 4 for the water-quenched alloy and for the samples isothermally transformed for the times shown. $R(q)$ is the ratio of magnetic to nuclear scattering intensity (equation 3). The theoretical value for VC is shown by the horizontal line.

Figure 6. SANS nuclear scattering data from the samples isothermally transformed at 700 °C following subtraction of Porod Law behaviour and incoherent scattering background. Transformation times shown by the symbols on the plots. (a) Plots of I versus q; (b) the corresponding Iq^2 versus q Kratky plots; (c) the first Guinier plot of $\ln(I)$ versus q^2; (d) the second Guinier plot of $\ln(q^2I)$ *versus* q^2.

Figure 7. Experimental SANS nuclear scattering data plotted as *I versus q* from samples transformed for the times shown (symbols) along with model fitted data (solid lines) using an oblate spheroid model with dispersion parameters of 0 and 0.2 for the polar and equatorial radii respectively.

Figure 8. Graphs to show the effect of isothermal holding time, t on particle dimensions obtained from Guinier analysis and model fitting. Data are shown for *R* (radius) and *T* (thickness) calculated from Guinier plots and *a* and *2b* from oblate spheroid model fitting. (a) is a plot of *R* and *a* (oblate spheroid major axis) versus time; (b) is a plot of *T* and *2b* (*b*= oblate spheroid minor axis) versus time. TEM measurements are radii calculated from major axis diameters.

.

Figure 9. (a) Effect of isothermal holding time, t, on precipitate number density (left hand axis) and volume fraction (right hand axis) determined from SANS data. (b) Effect of isothermal holding time, t, on measured microhardness, Hv, (left hand axis) and calculated yield strength increment (right hand axis). Error bars in Hv correspond to one standard deviation from the mean.

Table 1. Chemical composition of vanadium microalloyed steel in weight percent (wt%) and atomic percent (at%).

Table 2. Characteristics of the VX precipitates determined from analysis of SANS data for samples isothermally transformed at 700 °C for different times. R_{max}, R_g, R_{g1}, R_{g2}, and f_v are defined in section 3. $R(q)$ is the ratio of magnetic to nuclear scattering intensity.

Table 3. Average precipitate dimensions determined from analysis of SANS data for samples isothermally transformed for different times. R and T are the average radius and thickness of precipitate discs determined from the Guinier measurements of R_{g1}, R_{g2}. a and b are average equatorial and polar radii respectively from model fitting with an oblate spheroid. ($2b$ is polar diameter for direct comparison with T). σ_a is the dispersion parameter of a in model fitting.

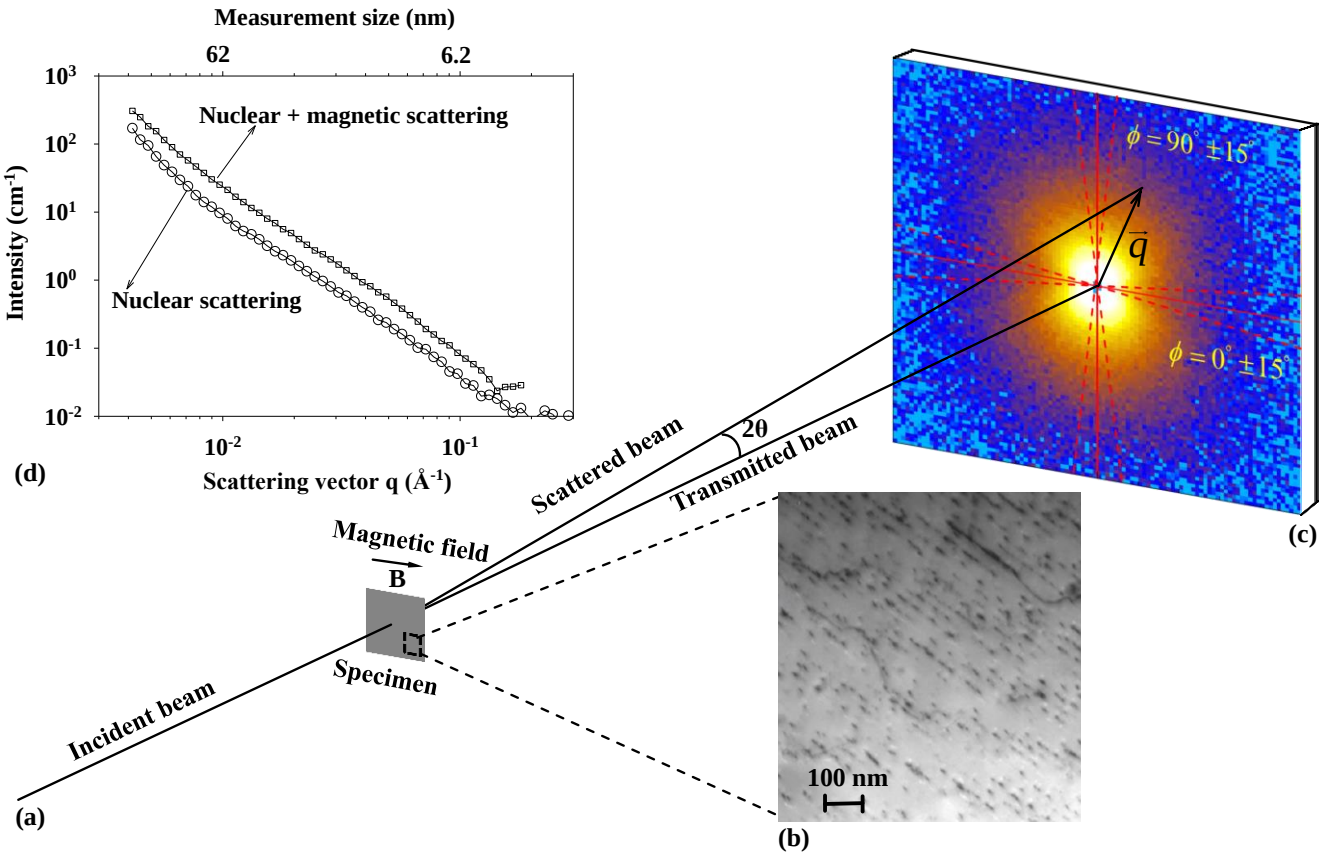

Figure 1. Experimental configuration used in the current SANS measurements. (a) An incident neutron beam transmitted through a specimen containing (b) nano-sized precipitates embedded in ferritic matrix. (c) The resultant SANS two-dimensional pattern in the presence of a horizontal magnetic field. (d) One-dimensional plot of the 'nuclear+magnetic' and nuclear scattering intensities.

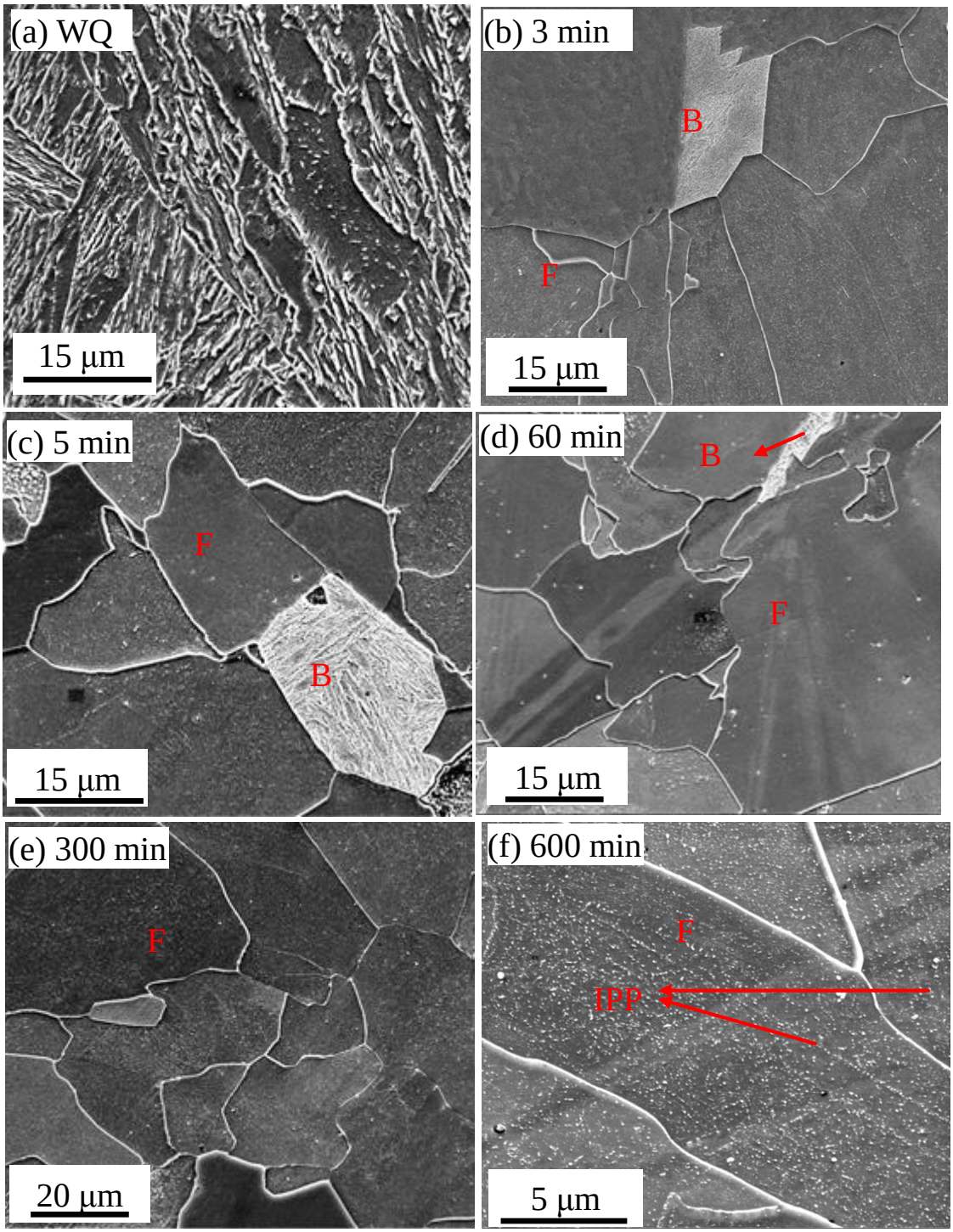

Figure 2. SEM images of the samples isothermally transformed at 700 °C for various times and water quenched. (a) directly water quenched; (b) – (d) isothermally transformed for 3, 5 and 60 min respectively showing ferrite grains (F) and regions of bainite (B) (transformed γ). (e) and (f) 300 and 600 min isothermal transformation times respectively. Coarsened interphase precipitates visible in (f).

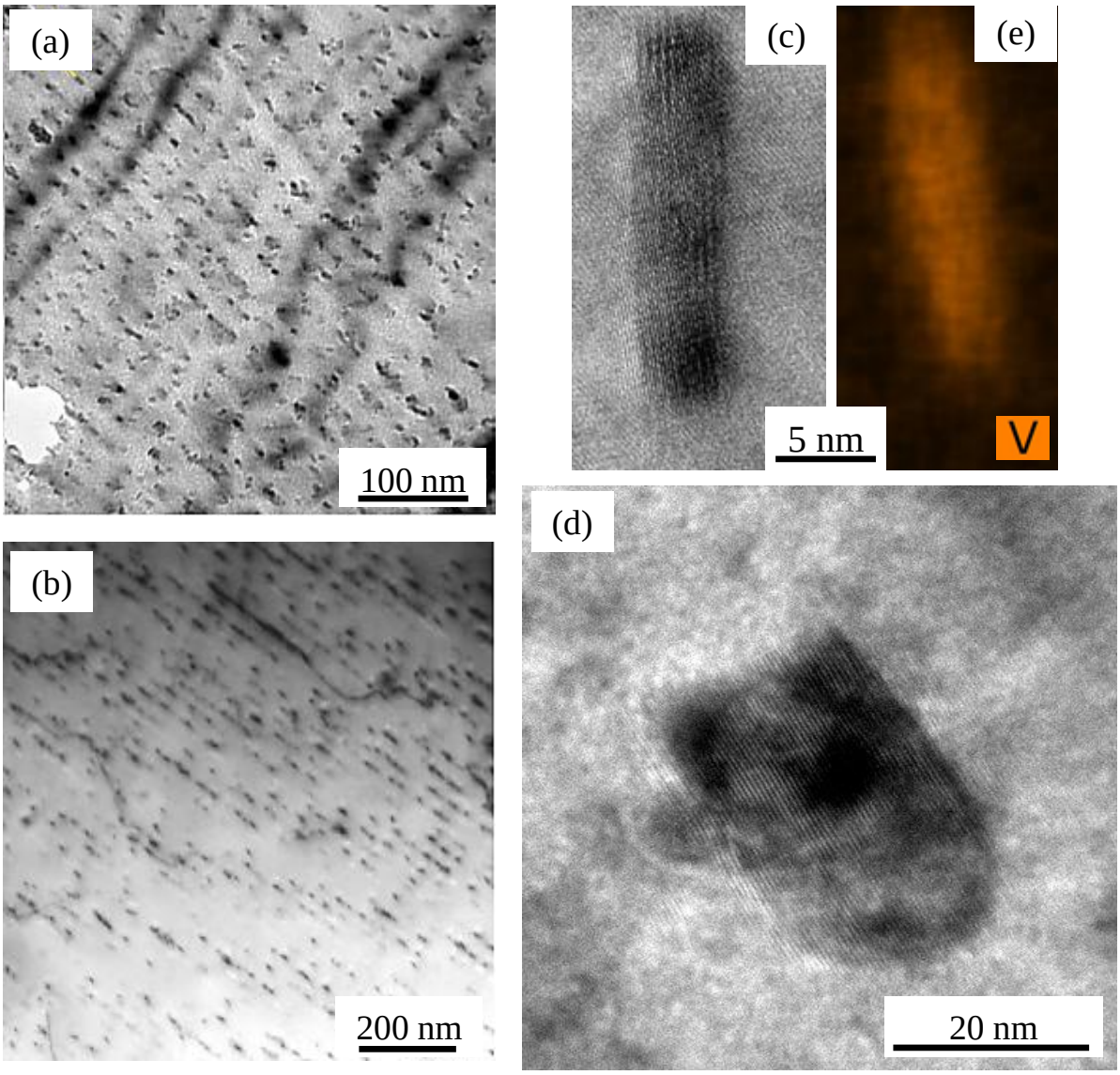

Figure 3. Bright field TEM images of periodic interphase precipitation taken from the samples isothermally transformed at 700°C for (a) 5 min and (b) 600 min. (c-d) High resolution TEM lattice image from the sample held for 600 min, (d) elucidating the disc nature of the precipitates and (e) EDX map for V.

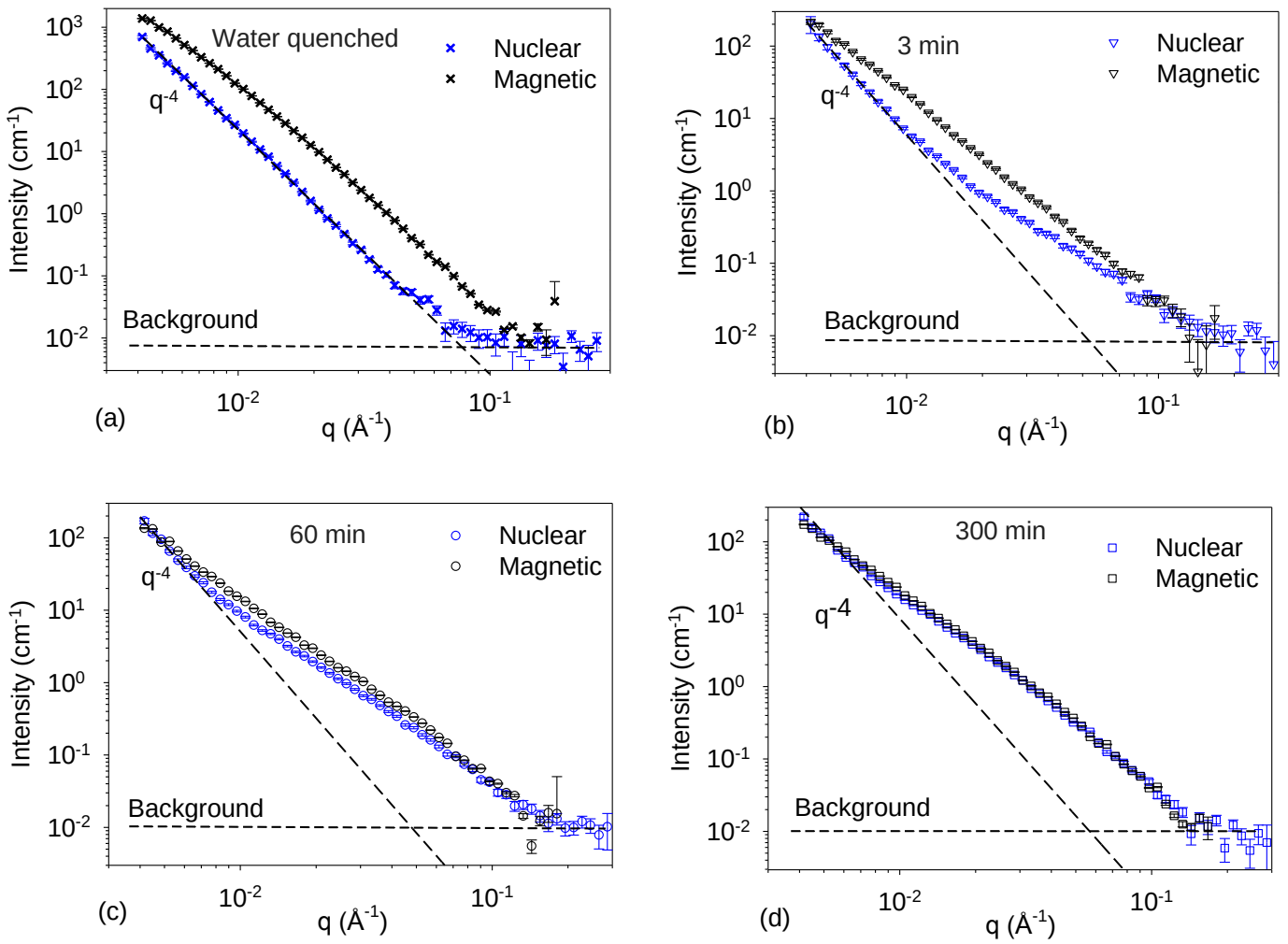

Figure 4. One-dimensional SANS patterns of intensity versus scattering vector obtained from the following samples: (a) water-quenched and (b) to (d) isothermally transformed. Transformation times for (b) 3 min, for (c) 60 min and for (d) 300 min. In (a), (b) and (c) there is a clear difference between nuclear and magnetic signals. In (d) they are virtually identical. Line of slope -4 is shown for reference on the log-log plot.

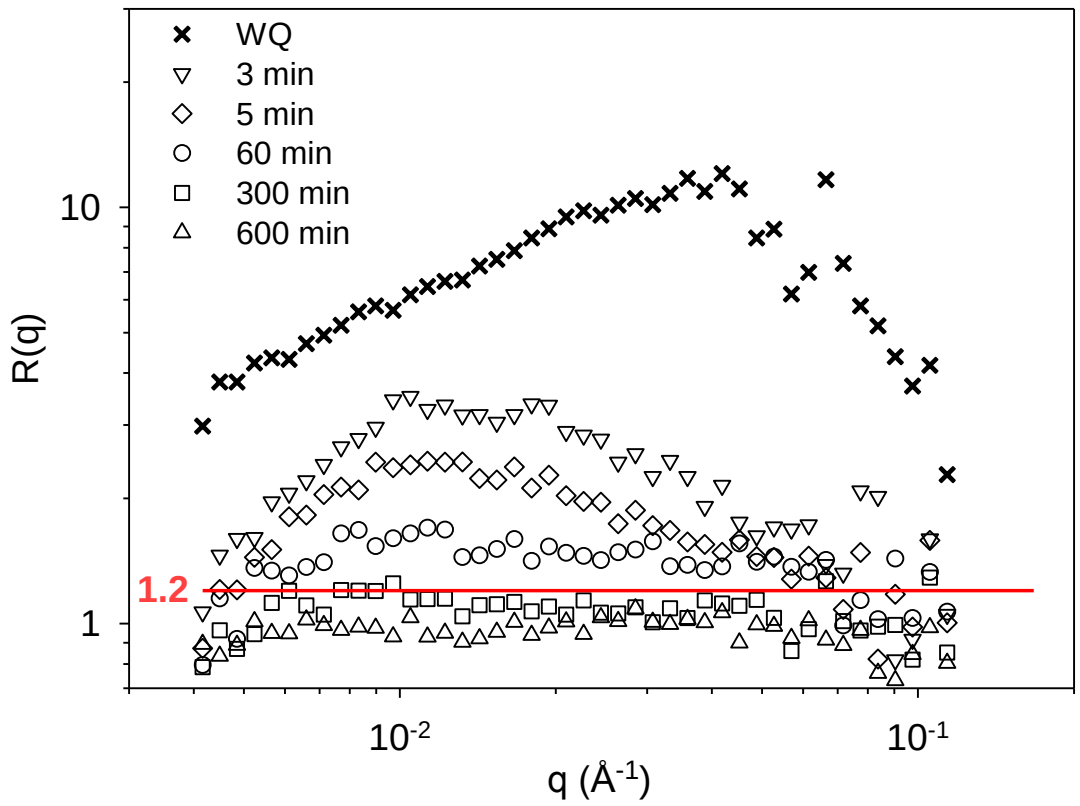

Figure 5. Plot of R(q) as a function of scattering vector calculated from the scattering curves in Fig. 5 for the water-quenched alloy and for samples isothermally transformed for the times shown. R(q) is the ratio of magnetic to nuclear scattering intensity(equation 3). The theoretical value for VC is shown by the horizontal line

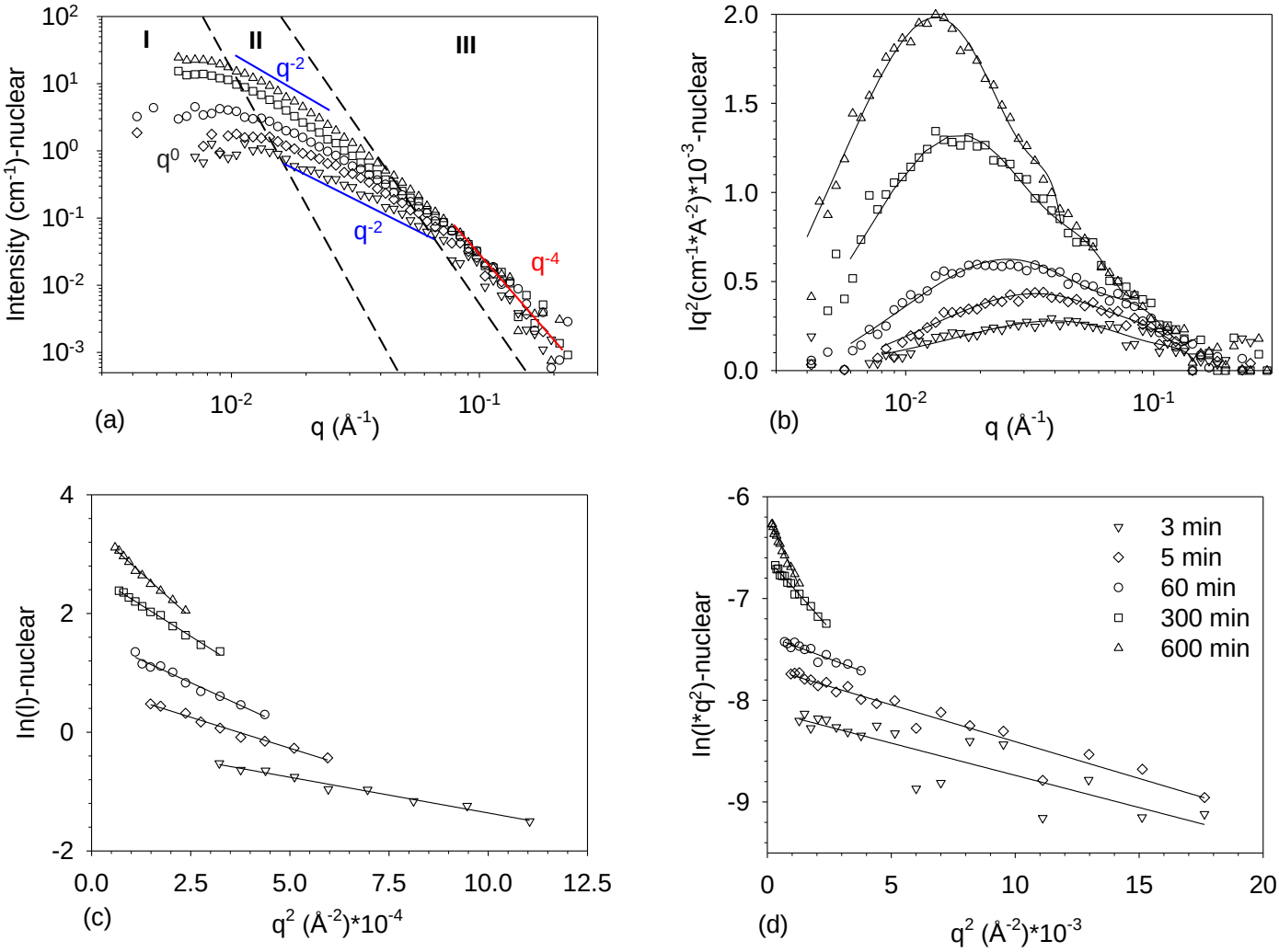

Figure 6. (a) SANS nuclear scattering data following subtraction of Porod behaviour and incoherent scattering background from the samples isothermally transformed at 700 °C for the times shown by the symbols; (b) the corresponding Iq^2 versus q Kratky plots (c) the first Guinier plot of ln(I) versus q^2 ; (d) the second Guinier plot of $\ln(q^2I)$ versus q^2.

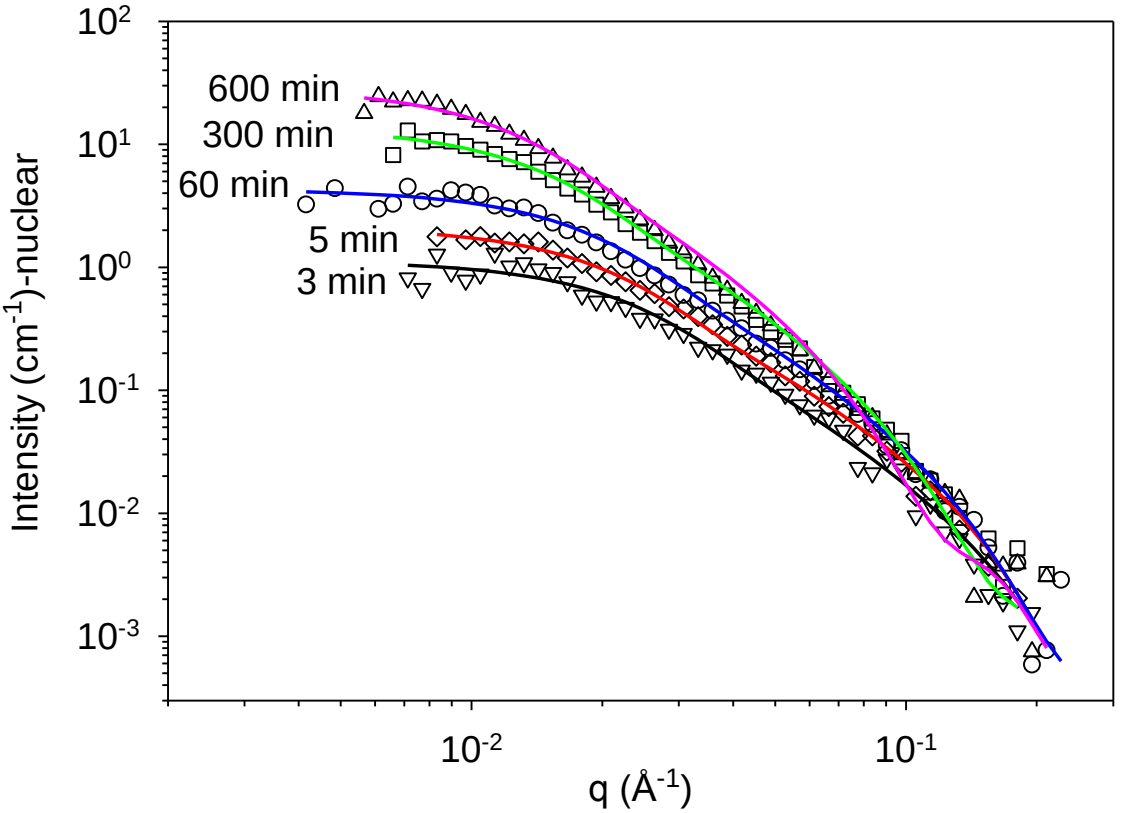

Figure 7. Experimental SANS nuclear scattering data plotted as *I versus q* from samples transformed for the times shown (symbols) along with model fitted data (solid lines) using an oblate spheroid model with dispersion parameters of 0 and 0.2 for the polar and equatorial radii respectively.

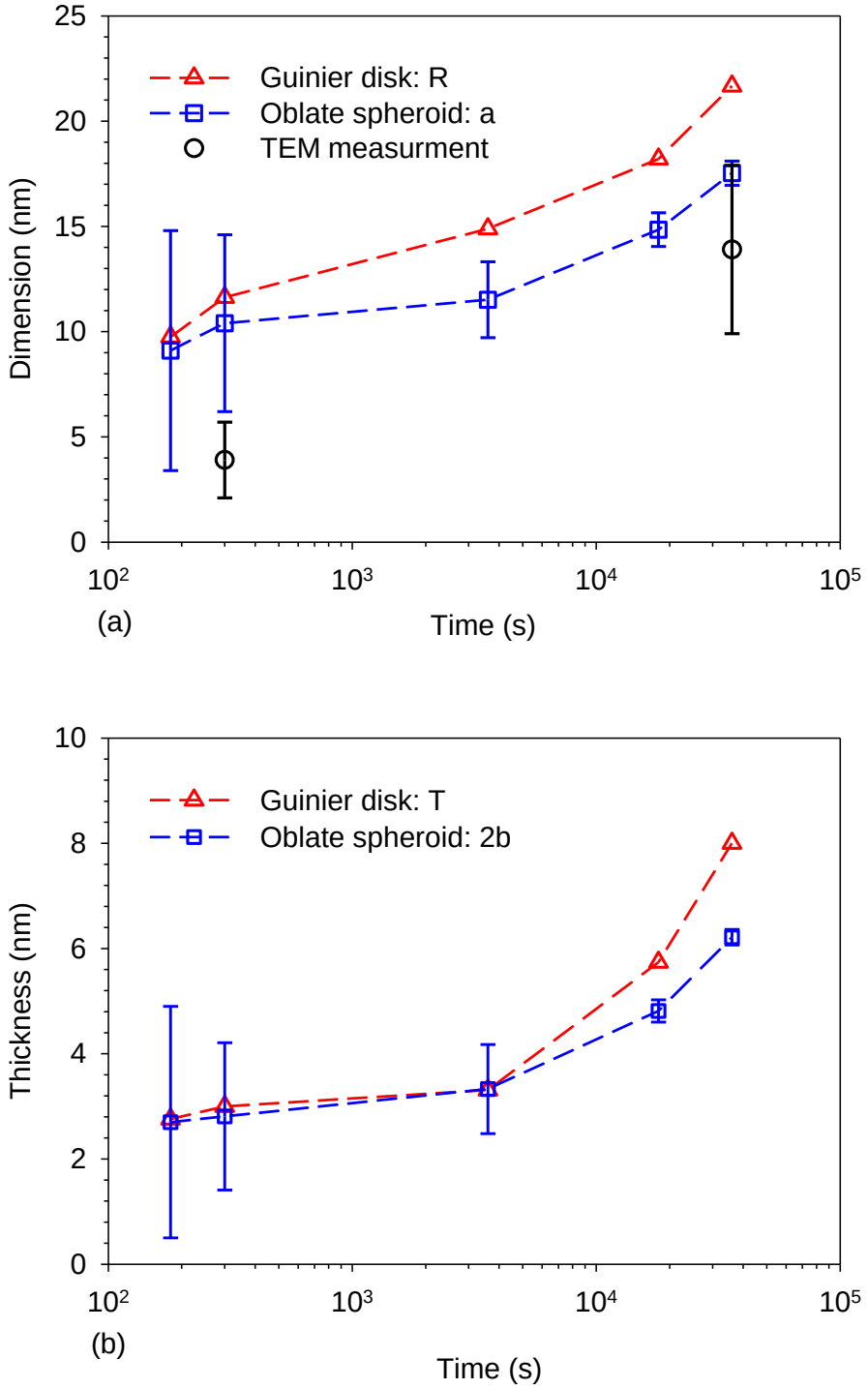

Figure 8. Graphs to show the effect of isothermal holding time, t on particle dimensions obtained from Guinier analysis and model fitting. Data are shown for R (radius) and T (thickness) calculated from Guinier plots and *a* and *2b* from oblate spheroid model fitting. (a) is a plot of *R* and *a* (oblate spheroid major axis) versus time; (b) is a plot of T and *2b* (*b*= oblate spheroid minor axis) versus time. TEM measurements are radii calculated from major axis diameters.

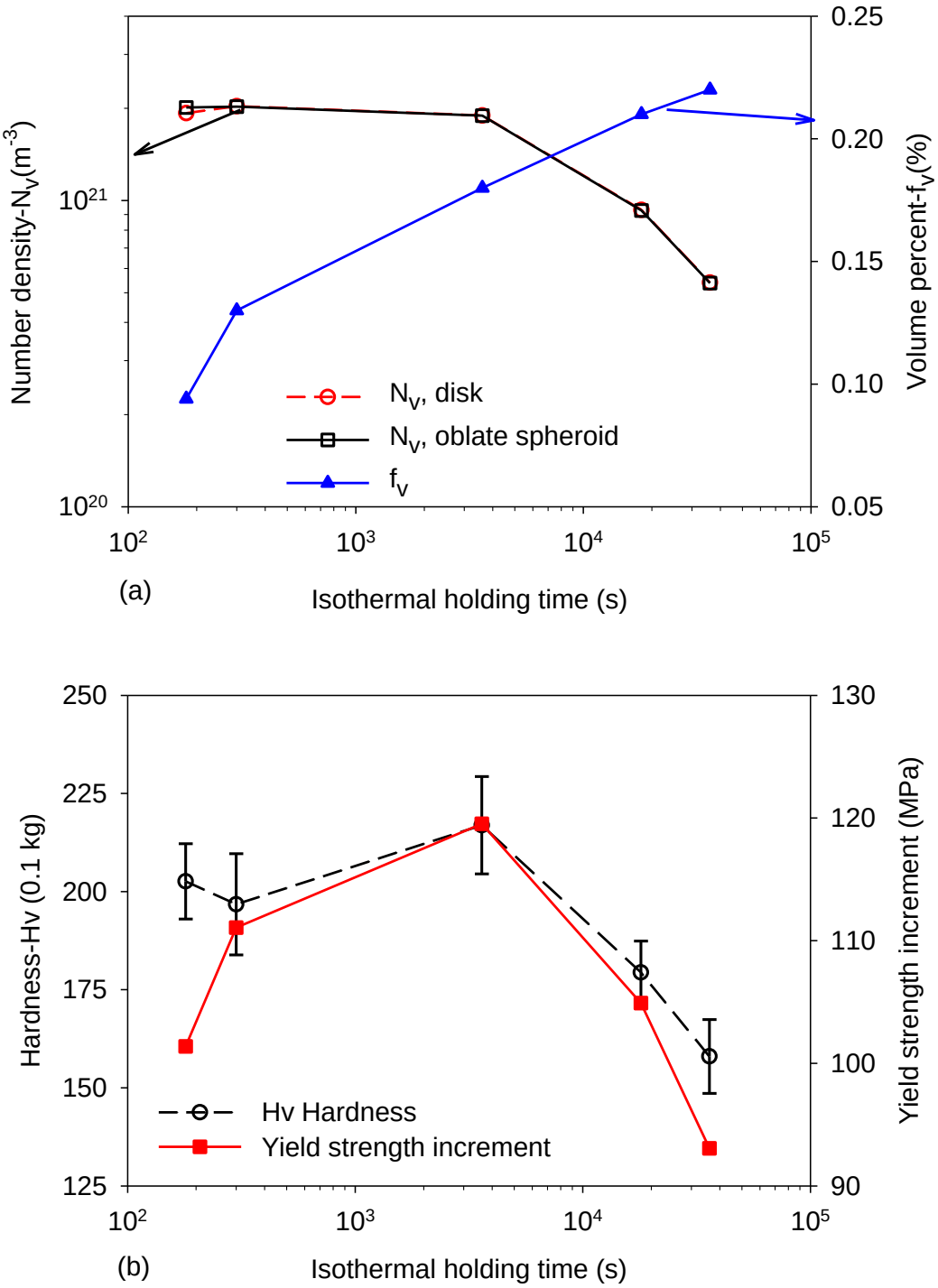

Figure 9. (a) Effect of isothermal holding time, t, on precipitate number density (left hand axis) and volume percent (right hand axis) determined from SANS data. (b) Effect of isothermal holding time, t, on measured microhardness, Hv, (left hand axis) and calculated yield strength increment (right hand axis). Error bars in Hv correspond to one standard deviation from the mean.

Table 1.

Chemical composition of vanadium microalloyed steel in weight percent (wt%) and atomic percent (at%).

	C	Mn	Si	Al	P	S	V	N (ppm)	Fe
wt%	0.047	1.60	0.18	0.043	0.013	0.005	0.20	50	Bal.
at%	0.22	1.62	0.36	0.009	0.023	0.009	0.22	200	Bal.

Table 2

Calculated precipitate characteristics determined from model-independent analysis of SANS data for samples isothermally transformed for different times. R_{g1}, R_{g2}, R_{max}, and f_v are defined in section 3. R(q) is the ratio of magnetic to nuclear scattering intensity.

Transformation time (min)	**R_{g1} (nm)**	**R_{g2} (nm)**	**R_{max} (nm)**	**Mean R(q)**	**f_v (%) (mean R(q))**	**f_v (%) (constant $\Delta\rho_{nuc}$)**
3	6.9	0.8	4.4	-	-	0.094
5	8.3	0.9	5.2	-	-	0.13
60	10.6	1.0	6.8	-	-	0.18
300	13.0	1.7	9.8	1.09	0.21	0.24
600	15.5	2.3	12.6	0.98	0.22	0.28

Table 3

Average precipitate dimensions determined from analysis of SANS data for samples isothermally transformed for different times. *R* and *T* are the average radius and thickness of precipitate discs determined from the Guinier measurements of R_{g1}, R_{g2}. *a* and *b* are average equatorial and polar radii respectively from model fitting with an oblate spheroid. (2*b* is polar diameter for direct comparison with T). σ_a is the dispersion parameter of *a* in model fitting.

Transformation time (min)	**Calculated from Guinier measurements**		**Oblate spheroid model fitting (σ_a =0.2)**	
	R (nm)	**T (nm)**	**a (nm)**	**2b (nm)**
3	9.8	2.8	9.1	2.7
5	11.6	3.0	10.4	2.8
60	14.9	3.3	11.5	3.3
300	18.2	5.7	14.8	4.8
600	21.7	8.0	17.5	6.2